Proceedings Paper:
El-Jummah, AM, Andrews, GE orcid.org/0000-0002-8398-1363 and Staggs, JEJ orcid.org/0000-0002-4970-4418 (2018) Enhancement of impingement heat transfer with the crossflow normal to ribs and pins between each row of holes. In: Proceedings of the ASME Turbo Expo 2018: Turbomachinery Technical Conference and Exposition. ASME Turbo Expo: Turbomachinery Technical Conference & Eposition GT 2018, 11-15 Jun 2018, Oslo, Norway. ASME . ISBN 978-0-7918-5108-1

https://doi.org/10.1115/GT2018-76969

ASME PROCEEDINGS PAPER

Enhancement of Impingement Heat Transfer with the Crossflow Normal to Ribs and Pins Between Each Row of Holes

Abubakar M. El-Jummah, Gordon E. Andrews, John E. J. Staggs
Paper No: GT2018-76969, V05AT10A006; 13 pages **https://doi.org/10.1115/GT2018-76969**
Published Online: August 30, 2018
Proceedings of the ASME Turbo Expo: Turbomachinery Technical Conference & Exposition GT2018
June 11 - 15, 2018, Lillestrom, Norway

ASME GT2018-76969

ENHANCEMENT OF IMPINGEMENT HEAT TRANSFER WITH THE CROSSFLOW NORMAL TO RIBS AND PINS BETWEEN EACH ROW OF HOLES

Abubakar M. El-Jummah
Department of Mechanical Engineering,
University of Maiduguri, P. M. B. 1069
Maiduguri, Borno, Nigeria

Gordon E. Andrews
School of Chemical & Process Engineering,
University of Leeds, Leeds,
LS2 9JT, UK

John E. J. Staggs
School of Chemical & Process Engineering,
University of Leeds, Leeds,
LS2 9JT, UK

ABSTRACT

Impingement heat transfer investigations with obstacle (fins) on the target surface were carried out with the obstacles aligned normal to the cross-flow. Conjugate heat transfer (CHT) computational fluid dynamics (CFD) analysis were used for the geometries previously been investigated experimentally. A 10 × 10 row of impingement jet holes or hole density, n, of 4306 m^{-2} with ten rows of holes in the cross-flow direction was used. The impingement hole pitch X to diameter D, X/D, and gap Z to diameter, Z/D, ratios were kept constant at 4.66 and 3.06 for X, D and Z of 15.24, 3.27 and 10.00 mm, respectively. Nimonic 75 test walls were used with a thickness of 6.35 mm. Two different shaped obstacles of the same flow blockage were investigated: a continuous rectangular ribbed wall of 4.5 mm height, H, and 3.0 mm thick and 8 mm high rectangular pin-fins that were 8.6 mm wide and 3.0 mm thick. The obstacles were equally spaced on the centre-line between each row of impingement jets and aligned normal to the cross-flow. The two obstacles had height to diameter ratios, H/D, of 1.38 and 2.45, respectively. Comparison of the predictions and experimental results were made for the flow pressure loss, ΔP/P, and the surface average heat transfer coefficient (HTC), h. The computations were carried out for air coolant mass flux, G, of 1.08, 1.48 and 1.94 kg/sm^2bar. The pressure loss and surface average HTC for all the predicted G showed reasonable agreement with the experimental results, but the predictions for surface averaged h were below the measured values by 5 – 10%. The predictions showed that the main effect of the ribs and pins was to increase the pressure loss, which led to an increased flow maldistribution between the ten rows of holes. This led to lower heat transfer over the first 5 holes and higher heat transfer over the last 3 holes and the net result was little benefit of either obstacle relative to a smooth wall. The results were significantly worse than the same obstacles aligned for co-flow, where the flow maldistribution changes were lower and there was a net benefit of the obstacles on the surface averaged heat transfer coefficient.

NOMENCLATURE

A	Impingement hole porosity = $((\pi/4)\ D^2)/X^2$
D	Impingement air hole diameter, m
G	Coolant Mass flux, kg/sm^2bar
h	Heat transfer coefficient (HTC), W/m^2K
H	Obstacle height, m
k_f	Thermal conductivity of fluid, W/mK
L	Test wall metal thickness, m
n	Number of jet hole/unit surface area, m^{-2}
N	Number of upstream rows of impingement holes
Nu	Nusselt Number
ρ	Density of air, kg/m^3
ΔP	Impingement wall pressure loss, Pa
P	Coolant supply static pressure (approx. 1bar)
Pr	Prandtl number
Re	Reynolds number (= $\rho V_j D/\mu$)
t	Obstacle thickness, m
T_∞	Coolant temperature, 288K
T^*	Normalized mean temperature, Eq. 1
T_S	Target surface metal wall temperature, K
T_w	Target wall imposed temperature (360K)
V_j	Impingement jet mean velocity, m/s

ν	Kinematic viscosity, m^2/s
W	Obstacle width, m
X	Hole to hole pitch, m
y^+	Inner variable wall normal coordinate ($\xi U\tau/\nu$)
Z	Plate to plate gap, m
ξ	Grid cell size, m

Subscripts

avg	Average	f	Fluid	h	Hole
c	cross-flow	j	Jet	∞	Coolant
L	Local	m	Mean	s	Surface
w	Wall	Z	Gap	o	Obstacle

Abbreviations

RW: Ribs Wall RP: Rectangular pin
ETSA: Enhanced target surface average
OSA: Obstacle surface average
STSA: Smooth target surface average

INTRODUCTION

Gas turbine (GT) wall cooling technologies often use impingement heat transfer and require that the design is optimized for effective wall cooling. Although impingement cooling is often combined with effusion cooling to enhance the internal wall cooling [1] for combustor wall cooling applications, there are potential advantages of using impingement only backside cooling in low NO_x combustors [2]. The main advantage of impingement only backside cooling is that with no film cooling air all the primary zone combustion air can pass through the low NO_x combustor after it has regeneratively cooled the combustor wall. With no combustor wall film cooling the primary zone operates leaner with lower primary zone temperature and lower NO_x emissions. This work was concerned with the enhancement of combustor impingement backside cooling using obstacles in the gap.

Impingement cooling creates a crossflow [3-6] which can interact with obstacles to enhance the overall cooling effectiveness. However, this is at the expense of increased impingement cooling pressure loss. A key difference between the use of impingement/effusion cooling and impingement only backside cooling is the air mass flow range that is used. For effusion cooling the minimum mass flow flux, G kg/sm^2bar, is required, but the impingement wall can have say 90% of the combustor pressure loss across it, with 10% of the overall pressure loss across the effusion wall, which will give low blowing ratios for good effusion cooling. A low G and high pressure loss impingement design gives a high X/D ratio and 12/1 is typical [4]. In contrast the backside impingement only cooling requires a very high coolant G set by the total combustor primary zone mass flow requirements [2]. Also, it must have a low pressure loss or there is no pressure loss left for the low NO_x flame stabilizer and this requires a low impingement X/D and 4.7 was used in the present work.

The problem with the high G low pressure loss design requirements for impingement backside regenerative cooling of low NO_x combustors, is that the impingement wall pressure loss can be of similar magnitude to the pressure loss of the crossflow along the impingement gap in the direction of the combustor air feed plenum chamber. This then results in a flow maldistribution between the impingement holes with the downstream holes having a higher G than the upstream holes [7-10]. This results in lower local heat transfer on the target wall at the upstream end of the impingement gap due to the lower G and higher heat transfer in the downstream section of the target wall due to the higher local G. If obstacles are then added in the gap to enhance the heat transfer then the increase in pressure loss can increase the flow maldistribution and increase the axial gradients in the heat transfer. It will be shown that this problem dominated the present CFD predictions and was the main reason for the predicted and measured relatively low influence of the obstacles normal to the crossflow on the overall surface averaged heat transfer.

The authors have previously investigated, using CHT CFD, the interaction of the crossflow with the obstacles aligned for co-flow with the minimum increase in pressure loss [7, 8]. This showed a lower influence on pressure loss and flow maldistribution with the ribs in co-flow. However, the increase in the heat transfer was small with a 20% improvement at low coolant flow rates for rectangular pin fin obstacles and 15% for rib obstacles. At high coolant flow rates the improvement was smaller at 5% for the rectangular pin fins and 1% for the rectangular ribs. The aim of the present work was to investigate whether these results could be improved on by using the crossflow transverse to the obstacles to create more turbulence and potentially a greater increase in the impingement heat transfer. The downside of this is the increase in pressure loss due to the higher blockage obstacles and consequent increase in flow maldistribution, as will be illustrated in the CFD results.

Studies of the influence of the impingement jet cross-flow with no obstacles present [3-6] shows that at high X/D with no flow maldistribution there is enhanced heat transfer to the cooled surface at the leading edge and reduced heat transfer at the trailing edge. These trends were predicted by El-Jummah et al. [4, 9-11] using 3D CHT CFD. This is a greater problem in wall cooling design for GT combustor walls as the distances to be cooled are greater than in turbine blades. These trends are the opposite of those discussed above for low X/D high G cases where flow maldistribution is the dominant effect.

The reasons for the deterioration in heat transfer with distance, at high X/D and high impingement pressure loss, are usually simply ascribed to the deflection of the impingement jet by the cross-flow [3]. CFD investigations of the aerodynamics in the impingement gap [4, 9-11] show that the effect of cross-flow was more complex. Its effect is linked to the impingement jet turbulence that covers only the downstream portion of the jet on the surface for the last few holes in the impingement gap. Also, the reverse flow jet from the impingement wall to the jet wall is deflected by the crossflow which reduces the efficient removal of heat, from the cooled surface and increases the transfer of heat to the impingement jet surface [4, 9-11].

Andrews et al. [13-15] experimentally used the test rig of Figure 1 and the test walls of Figure 2 as typical obstacle (fins) walls. The present CHT CFD work investigates their experimental results, whereby two types of obstacles: ribs wall as in Figure 2a and rectangular pins of 2b were investigated. This work investigates the alignments of the cross-flow configuration as Figure 2 shows. El-jummah et al. [7, 8] investigated the co-flow design. The obstacle heights for pins were higher than for ribs, so as to have the same flow blockage for the pins and ribs and hence the same pressure loss. Experimentally the obstacle walls were machined from a solid block of stainless steel and there was no joint or thermal resistance from the wall to the obstacles.

El-jummah et al. [7] have reviewed the published work on the influence of obstacles in the impingement gap on the heat transfer. Obstacles that have been investigated are ribs, rectangular or cylindrical pin fins, inclined pin-fins, inclined rectangular pin-fins, dimples, bumps and perforated ribs. There may be one obstacle per impingement jet (most common) or arrays of obstacles per impingement jet (best enhancement). The literature [7], on the addition of various turbulators in the impingement gap, shows that enhancing the already high impingement heat transfer is quite difficult and typically a 20% enhancement would be a good performance.

Shizuya and Kawaike [16] developed probably the highest enhancement of plane wall impingement heat transfer. They investigated a wide range of enhanced impingement cooling configurations and the most effective had 50% improvement in heat transfer. The obstacles used were several cylindrical pin-fins in a square array for each impingement jet. They investigated X/D of 4 and 8 and found the same 50% enhancement for both geometries. This data was for 20 rows of impingement holes and was the surface average effect. Their use of several pin-fins per impingement hole was the first to show 50% enhancement of impingement heat transfer and remains today the best enhancement of surface averaged impingement heat transfer in the literature. More recently Azad et al. [17] have also shown that using five pin fins per impingement jet, for a 4 × 12 impingement hole array, gave a high enhancement of the plane duct impingement heat transfer.

Ligrani et al. [18] and Ligrani [19] reviewed heat transfer enhancement as applied to internal cooling of turbine components. They found that ribbed wall obstacles gave the best heat transfer enhancement. In the present work ribbed fins were compared with long plane fins with the impingement gap flow aligned as a crossflow over the fins, as shown in Fig. 2.

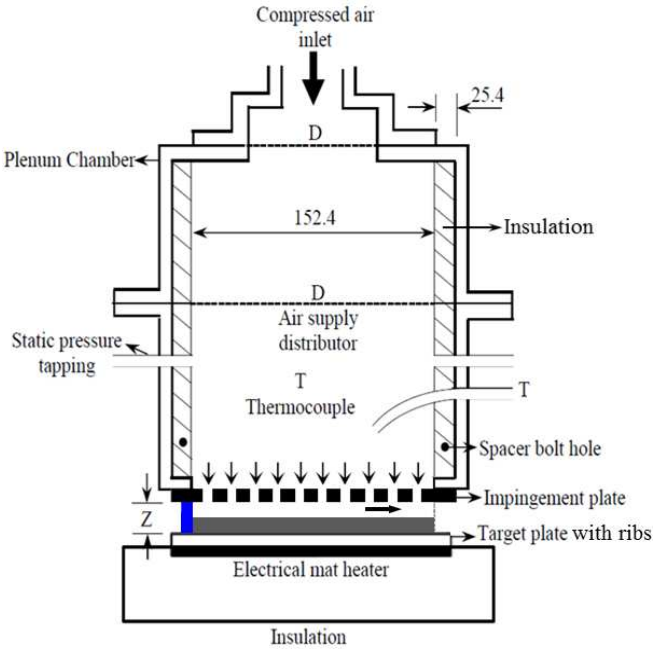

Figure 1: Impingement jet ribs wall experimental test rig [7]

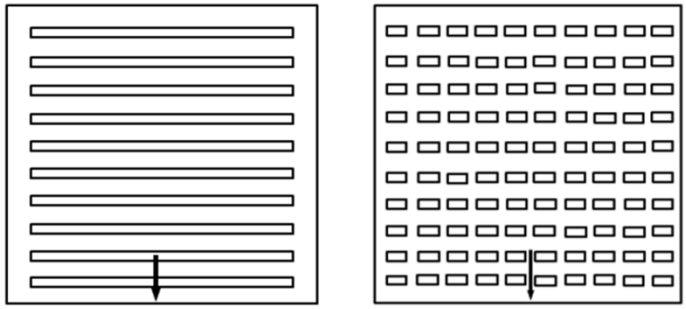

Figure 2: Experimental target plate with obstacle walls [12-14]

Table 1 Geometrical Parameter

Variables	Dimensions
D (mm)	3.27
X (mm)	15.24
Z (mm)	10.0
L (mm)	6.35
L/D	1.94
X/D	4.66
Z/D	3.06
X/Z	1.52
n	4306 m^{-2}
Array	10 × 10

Table 2 Obstacle Walls Parameters

Types	W (mm)	H (mm)	t (mm)	H/W
RW: cross-flow	continuous	4.50	3.0	
RP: cross-flow	8.59	8.0	3.0	0.93

EXPERIMENTAL CONFIGURATIONS

The present square array hole impingement cooling geometries are summarized in Table 1. They have the same configurations as those used for the work of the authors for smooth target wall impingement cooling [4, 10, 17]. Table 2 also summarizes the obstacle walls geometries and the cross-flow velocity values. These obstacles were those investigated experimentally by Andrews et al. [13, 14] and Abdul Hussain and Andrews [15]. The 2mm gap between the top of the rectangular pin was to allow for thermal expansion as the target and obstacle are hotter than the impingement wall. The aim was to reduce thermal gradients relative to those where the pin was thermally connected to the two walls at different temperatures.

The impingement configurations were for single sided impingement gap exit air flows, with the obstacle walls configured midway between the impingement jet holes and aligned in the cross-flow direction. The previous work with co-flow [7] showed a significant increase in the overall surface averaged heat transfer. This was well predicted and measured with rectangular pin-fins with a 20% improvement at low coolant flow rates for the rectangular pin fin obstacles and 15% for the ribs. At high coolant flow rates the improvement was smaller at 5% for the rectangular pin fins and 1% for the rectangular ribs.

The coolant mass flux, G, was varied from 1.08 - 1.93 kg/sm^{2}bar, this is the range of G relevant to regenerative combustor wall cooling in low NOx gas turbines [7, 10]. For low NO_x gas turbine combustors if all the combustion air is used for wall cooling prior to feeding the low NO_x combustion zone, then G is typically 2 kg/sm^{2}bar. If effusion of impingement effusion cooling was used then a very low G is required and 0.1 – 0.2 g/sm^{2}bar is the typical range used. The gives low blowing ratios on the effusion cooling holes and enhanced film cooling effectiveness [1].

The experimental results expressed the measured surface averaged heat transfer coefficient as a function of the coolant mass flux, G, kg/sm^{2}bar. The term gives the coolant mass flow that is being used to cool a fixed surface area of the combustor or turbine blade wall. G is proportional to the mean velocity, V, over the entire surface area to be cooled at a constant air coolant temperature. For a transpiration or porous wall this mean velocity has direct application. Eq. 1 gives the derivation of the relationship between the present definition of G and the mean surface averaged velocity, V.

Mean surface velocity $V = m' / (\rho A) = m' RT / PA$

Thus $V/RT = m'/PA =$ kg/(sm^{2}Pa)

$V10^5/(RT) = m'/PA =$ kg/(sm^{2}Bar) = G (1)

Eq. 1 gives for a G of 0.5 kg/sm^{2}bar a mean surface velocity at 700K coolant temperature of 1.0 m/s. The use of the coolant mass flow in terms of G enables the results at atmospheric pressure to be applied at engine pressures. With impingement cooling, the air velocity in the holes is defined by G and the hole area and is constant irrespective of the pressure. The G investigated and the associated impingement hole velocities and Re are summarized in Table 3.

The crossflow velocity, U_c, in Table 3 is that at the discharge end of the duct based on the full impingement gap flow area in the absence of the obstacles. In the plane of the minimum flow area of the obstacles the mean crossflow velocity after the last impingement hole was increased due to the obstacle area blockage. This was for co-flow a blockage of 9.8% for the continuous rib and 15.7% for the slotted rib [7] and for the present work was 45% for the continuous ribs and the slotted ribs.

The same blockage was used for the two rib geometries as the pressure loss penalties would be similar, but the heat transfer changes could be different. The ribbed geometry would keep the high velocity flow adjacent to the impingement target wall and this might lead to greater heat transfer enhancement. The higher crossflow blockage was anticipated to give higher local velocities, greater turbulence generation and higher heat transfer, compared with the co-flow geometry. However, any benefits of these high local velocities would be offset by increased pressure loss relative to the co-flow geometry. The measured flow pressure loss for the plane impingement wall is also given in Table 3. The Mach numbers for the impingement

Table 3 Flow Conditions

G (kg/sm^{2}bar)	1.93	1.48	1.08
V_i (m/s)	43.41	33.5	24.3
Jet Mach No.	0.13	0.10	0.07
U_c (m/s)	24.0	18.4	13.4
V_i/U_c	1.8	1.8	1.8
$Re_h \left(=\rho V_j D/\mu\right)$	9680	7440	5400
$\Delta P/P\%$	2.2	1.3	0.7
T_∞(K)	288	288	288
T_w (K)	353	353	353
ρ (kg/m^3)	1.225	1.225	1.225

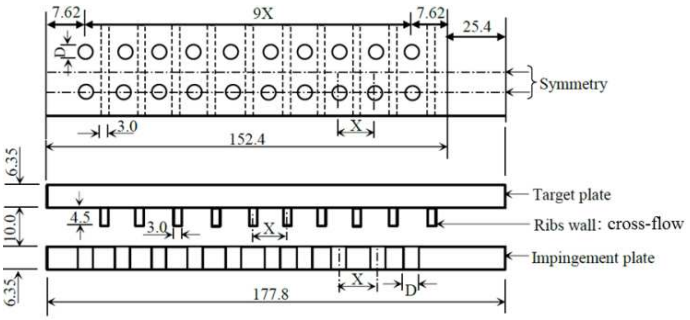

Plan and side view of the symmetries

Figure 3: Symmetrical elements of the computational grids

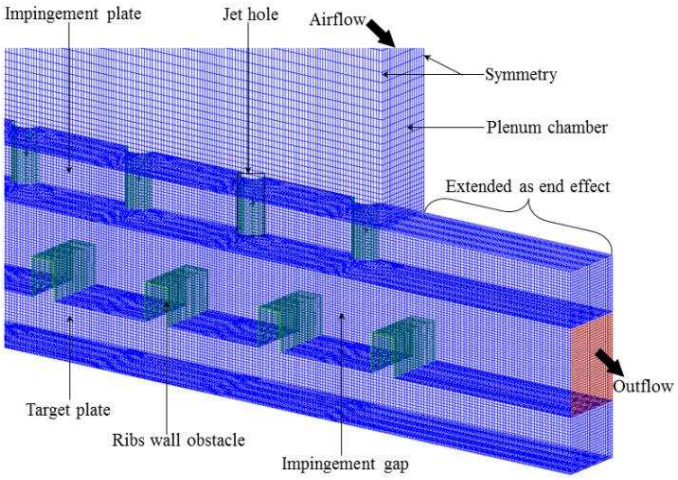

Figure 4: Obstacle walls grid model geometry in cross-flow

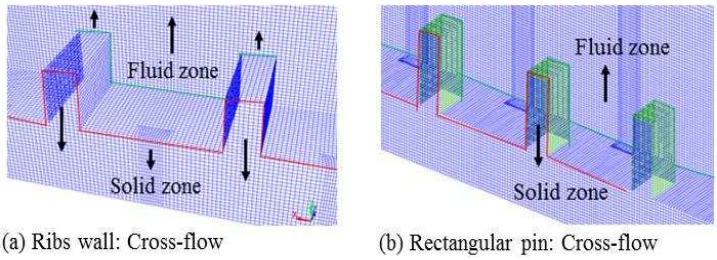

(a) Ribs wall: Cross-flow (b) Rectangular pin: Cross-flow

Figure 5: The ribs and pins grid modelled obstacles

Table 4 Percentage of grids cells for y^+ ~35

Types	Cells % of total number of cells			
	Test walls	Obstacles	Gap	Holes
RW: cross-flow	28.5	8.1	19.7	8.4
RP: cross-flow	28.5	7.2	20.6	8.4

jets are given in Table 3 and were all <0.2 which means that incompressible flow CFD can be used.

CFD METHODOLOGY

Figure 3 show the computational structural model grid that was created using symmetrical representation of the computational grids in Figure 4, while Figure 5 shows the grids for the two obstacles. Figure 5 is for the ribs wall of the cross-flow obstacle shown in Figures 2 and 3, which is one row of impingement half holes that was generated using the ANSYS ICEM tool. Entirely new model grid geometries were created as G was varied [7].

The geometries for each cross-flow grid walls were developed on the symmetry plane between holes, which includes half the pin obstacle or 10 % for the ribs; therefore each obstacle was modelled using the whole of its obstacle width. Table 4 show the percentage of cells created in each part of the individual model grid obstacles at a fixed G of 1.93 kg/sm^{2}bar. The total number of cells was 1.35×10^6 for low G and ~ 1.45×10^6 for the highest G.

Model Computation and Procedures

The predicted co-flow model configurations by El-jummah et al. [7] employed the standard k - ε turbulence (or high Re) model [19] in the ANSYS Fluent code. Their work showed good agreements with the measured surface averaged heat transfer and the measured pressure loss. This work applied the same computational procedures, which incorporated both fluid and solid zones analysis as in Figures 4 and 5. The Fluent solver was based on y^+ value ~35 near the wall ($30 < y^+ < 300$ or the law of the wall) using standard wall functions.

The convergence criteria were set at 10^{-5} for continuity, 10^{-11} for energy and 10^{-6} for k, ε and momentum (x, y and z velocities), respectively. The minimum cell orthogonal quality and aspect ratio, for all the geometries modelled were fixed at 0.61 and 3.53, respectively. The numbers of cells in all the computational zones were shown to be adequate, which was based on the previously predicted grid sensitivity tests [7, 10, 11]. The second-order and first-order discretization schemes for the momentum and TKE/dissipation respectively using the PISO schemes that were based on PRESTO applications have been employed. The stability of the solutions was also carried out using the transient state solution, which were conducted after convergence.

COMPUTATIONAL RESULTS

Predictions of the Aerodynamics

The predicted flow aerodynamics are shown in Figure 6 for the ribs, pins and smooth wall for the first two impingement holes (upstream) and for the last two impingement holes in the 10 hole array (downstream). For the smooth wall Figure 6 shows that for the first two rows of impingement holes the flow interaction was as expected with the first and second impingement jet flowing across the target surface and interacting to produce a reverse flow jet in line with the centre of four impingement jets. However, with the build up of the crossflow by the end two impingement holes the aerodynamics were very different and were dominated by the crossflow and the reverse flow jet was stongly tilted in the downstream direction. The aim of using rib obstacles was to place them so that both sides were scrubbed by the reverse flow jets. Figure 6a shows that this was achieved for the first two ribs, but at the expense of removing the strong aerodynamic surface jet interaction with its generation of surface turbulence. Figure 6a shows that the main impact of the continuos rib with 45% blockage was to increase the cross flow velocity in the impingement gap. This resulted in more deflection of the impingement jets as shown in Figure 6a for the last two holes downstream holes. This shows the high crossflow velocity that is not in contact with the cooled wall due to the blockage of the

rib. Not surprisingly this results in poor cooling of the target surface, as will be shown later.

The rectangular pins give the expected aerodynamics for the first two rows of hole. The pins were place in the centre of the reverse flow in Figure 6c and their faces were scrubbed by the reverse flow. There was clearly flow acceleration into the gap between the pins and this high velocity was in contact with the surface to be cooled. However, now the crossflow jet is directly in line with the impingement jet and its deflection is clear by the second jet in Figure 6b. By the downstream two holes the crossflow totally dominates the flow and there is no impingement jet penetrating to the surface. However, the crossflow is predicted to generate a recirculating flow on the target surface and this should benefit the heat transfer. From these aerodynamics it could be predicted that the action of the ribs and pins in crossflow is likely to be to reduce the surface heat transfer as it makes the crossflow dominate the impingement flow.

Another key feature of the aerodynamics is that the pressure loss due to the cross flow induces a flow maldistribution between the upstream and downstream impingement jets, as discussed above. This was predicted by integrating the predicted hole velocity on the mid plane of the impingement holes, shown in Figure 4. These mid plane mean velocities were then divided by the mean velocity based on the mass flow rate G being equally split between all the holes. These normalized impingement jet velocities are shown as a function of the hole number in Figure 7 for G=1.93 kg/sm^{2}bar. This shows that a major effect of the obstacles normal to the crossflow was to increase the flow maldistribution. For the smooth duct this was

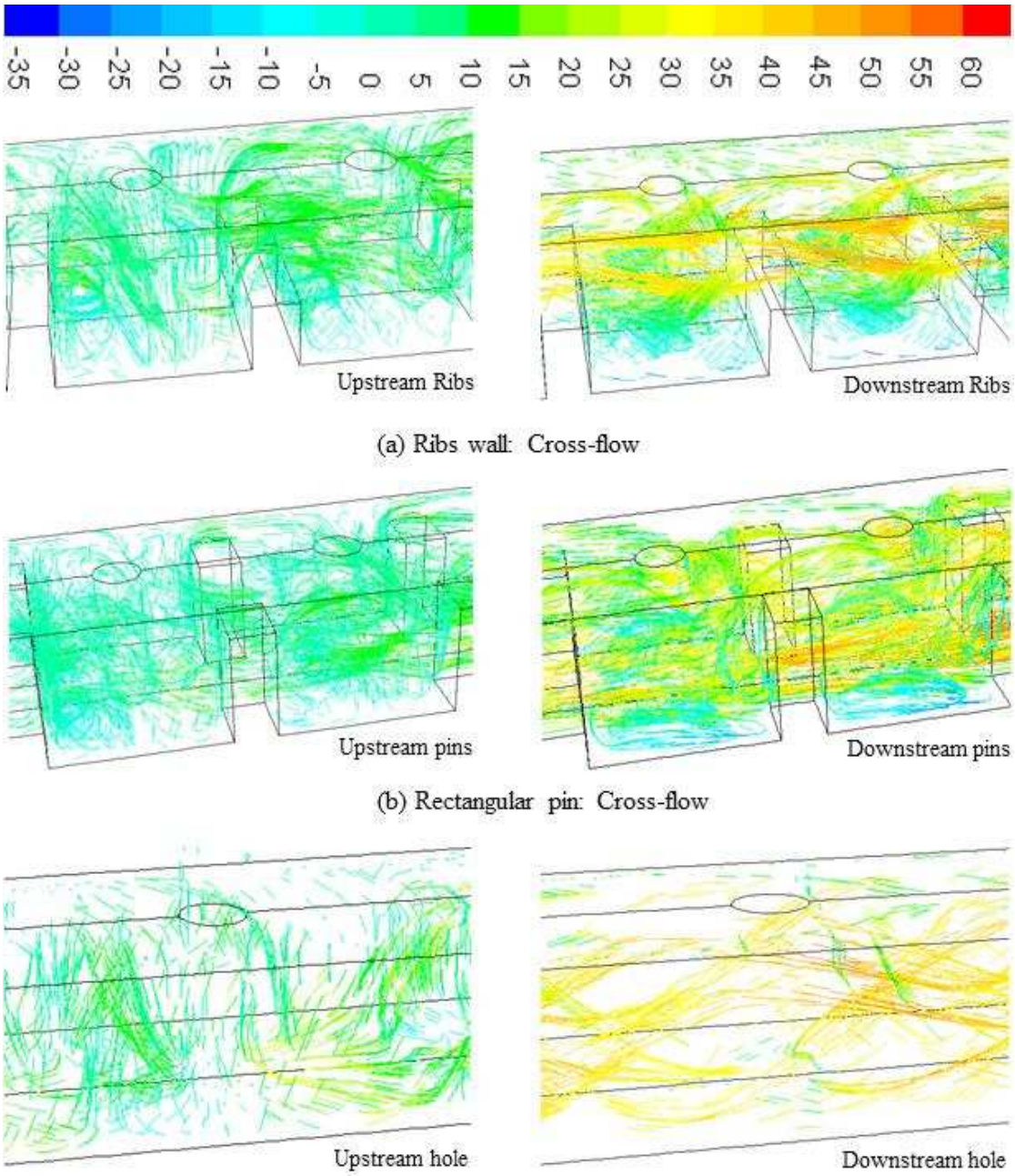

Figure 6: The impingement gap velocity (m/s) path lines for the two obstacles and the smooth target geometries for G = 1.93 kg/sm^{2}bar

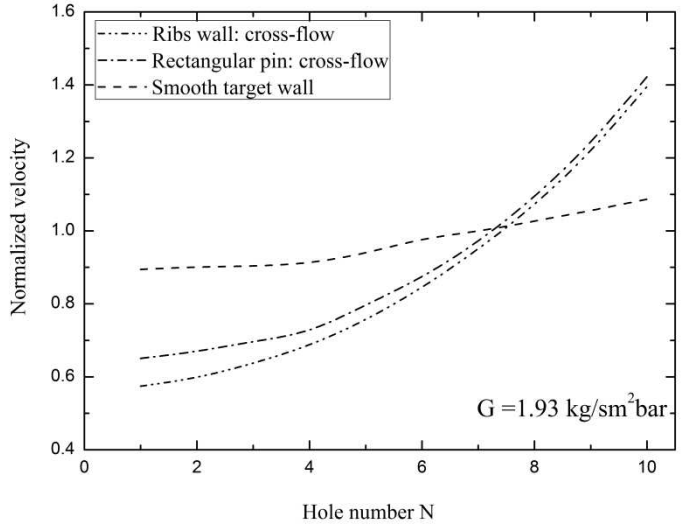

Figure 7: Predicted comparison of impingement jet holes flow-maldistribution for the obstacle and smooth wall geometries

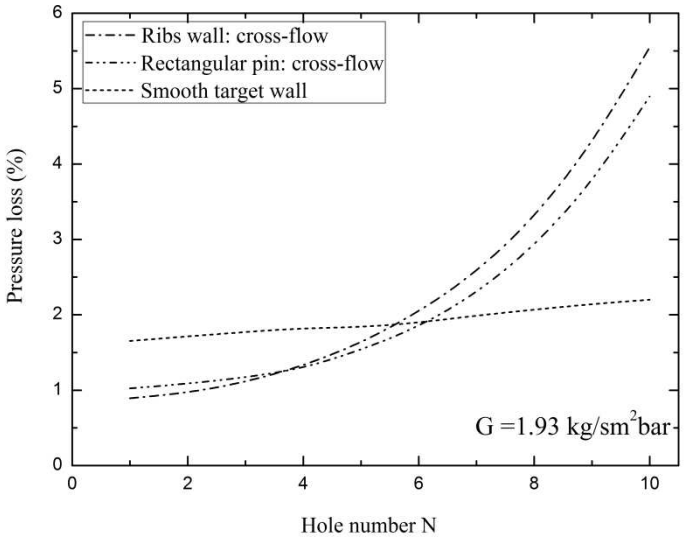

Figure 8: Predicted comparison of impingement jet holes surface static pressure loss for the obstacle and smooth wall geometries

a relatively small effect of -10% flow for the first hole and +10% for the last hole and with the obstacles this was increased to -40% for the first hole and +40% for the last hole. It will be shown later that this increased flow maldistribution dominates the influence on the surface heat transfer distribution.

Figure 7 shows that the flow maldistribution for the continuous rib and the rectangular pins were very similar, in spite of the large differences in their aerodynamics shown in Figure 6. This is because the flow blockage was the same with a similar change in pressure loss that drives the flow maldistribution. The flow maldistribution was a little higher for

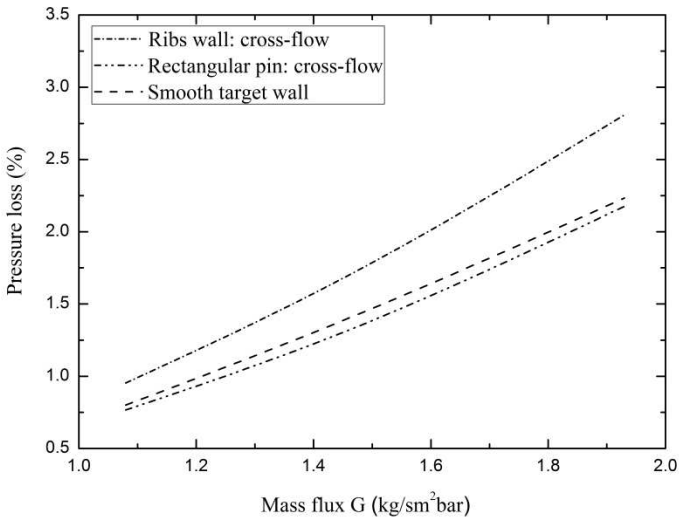

Figure 9: Predicted comparison of impingement gap exit flow pressure loss for the obstacle and smooth wall geometries

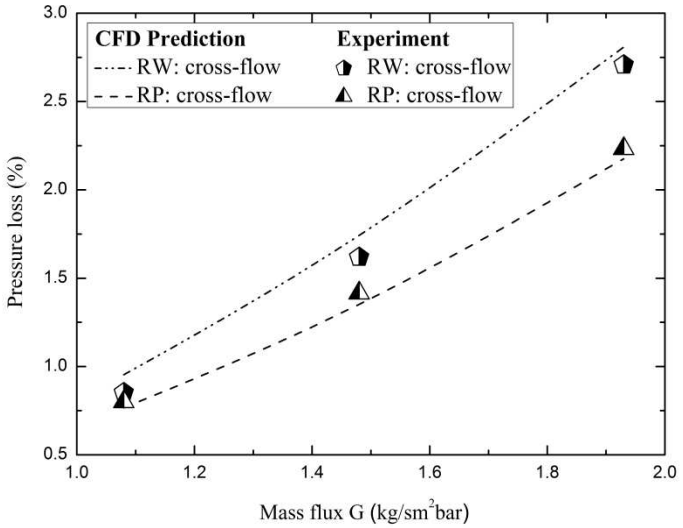

Figure 10: Comparison of predicted and measured impingement gap exit flow pressure loss for all G of the obstacle geometries.

the continuous ribs compared with the pins, but both were much higher than for the smooth wall. The reason for the greater flow maldistribution is considered to be due to the continuous high velocity crossflow above the ribs with reduced recirculation below, as shown in Figure 6.

The predicted axial variation of the static pressure loss on the centerline of the impingement wall surface between the impingement jets is shown in Figure 9 for a G of 1.93 kg/sm^{2}bar. For the smooth wall the increase in pressure gradient along the impingement gap flow was small at about 1.7% to 2.2% or 0.5% due to the crossflow. With the obstacles in the gap in the crossflow the flow maldistribution gave a reduced pressure loss at the first hole and much increased pressure loss at the last hole.

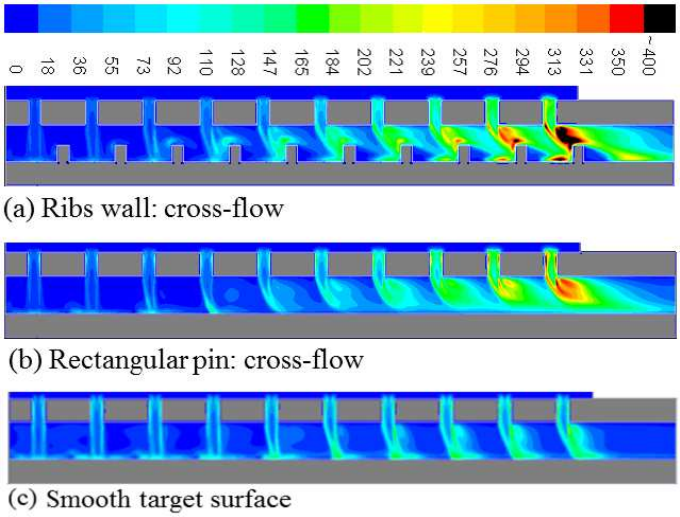

Figure 11: Comparison of predicted TKE (m^2/s^2) contours along the plane of impingement gap row of half holes for cross-flow obstacles with smooth wall

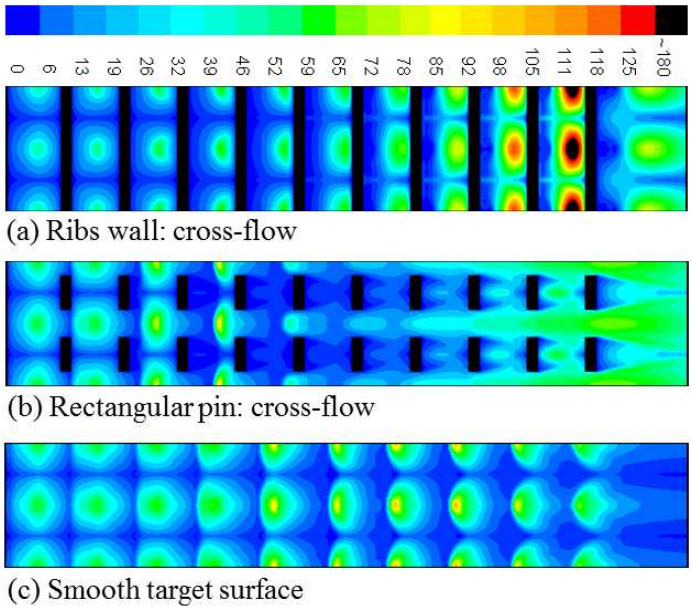

Figure 12: Comparison of predicted TKE (m^2/s^2) contours for enhanced and smooth surfaces for G of 1.93 kg/sm^{2}bar

The pressure loss increased from 1% to 5.5% along the impingement gap, which is 10 times the pressure loss change for the smooth wall.

The predicted overall pressure loss was determined from the plenum chamber to the crossflow extended discharge, as shown in Figure 4. This extended region of the impingement gas was necessary to predict the static pressure recovery from the expansion from the crossflow gap, to give the same aerodynamics as in the measurements, which had this extended region at the gap outflow. This static pressure recovery is not shown in Figure 8 or included in the pressure loss predictions in

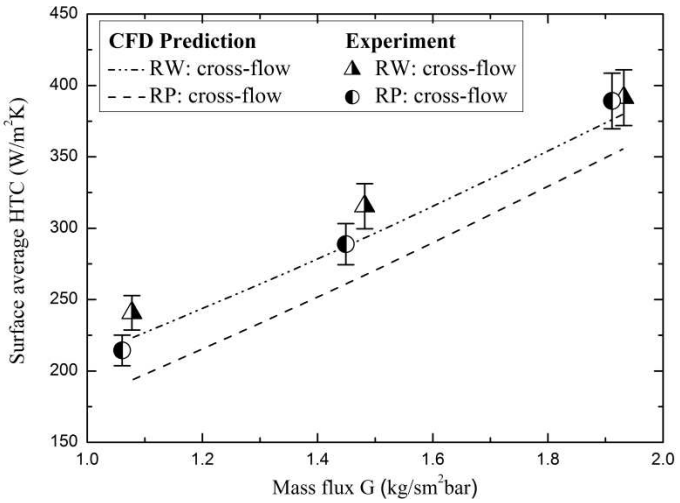

Figure 13: Comparison of predicted and experimental HTC on the target surface for all G of the obstacle model geometries

Figure 9, as the gap distance shown does not include the full outlet region. The predicted overall pressure loss, including the pressure recovery outlet region, is shown as a function of G in Figure 10, where the predictions are compared with the measurements. The predictions were a little high for the continuous ribs and in good agreement for the rectangular pins. This indicates that the aerodynamics were reasonably predicted. The pressure loss is controlled mainly by the impingement jet hole inlet flow separation and reattachment inside the hole, as well as by the extra pressure loss of the crossflow as discussed above. The 90^o turn of the flow in the impingement gap has a pressure loss of about 1 dynamic head, which is the same as the hole exit pressure loss in the absence of the target wall [20].

The final aerodynamic predictions that will be present are for the turbulent kinetic energy (TKE), for which no measurement exists. These are shown in Figure 11 in the plane of the centerline of the impingement jet and in Figure 12 for the target surface TKE distribution. Figure 11 shows the decreased turbulence in the first impingement jets compared with the smooth wall case, due to the decreased flow caused by the flow maldistribution. The higher turbulence in the downstream jets due to the higher flow is also clear for the predictions for both obstacles. Figure 11b shows that the large crossflow caused by the obstacle blockage prevents the impingement jets from reaching the target surface, which means that heat transfer will be impaired compared with the smooth surface. This is shown in Figure 12b for the surface distribution of the TKE, where there are no high spots of TKE in line with an impingement point. Figure 11a shows that for the ribs the flow maldistribution leads to very high TKE for the tenth obstacle. It also shows that the region of high TKE is against the upstream side of the rib. It will be shown later that the surface Nu distribution is very similar to the plots of surface TKE distribution.

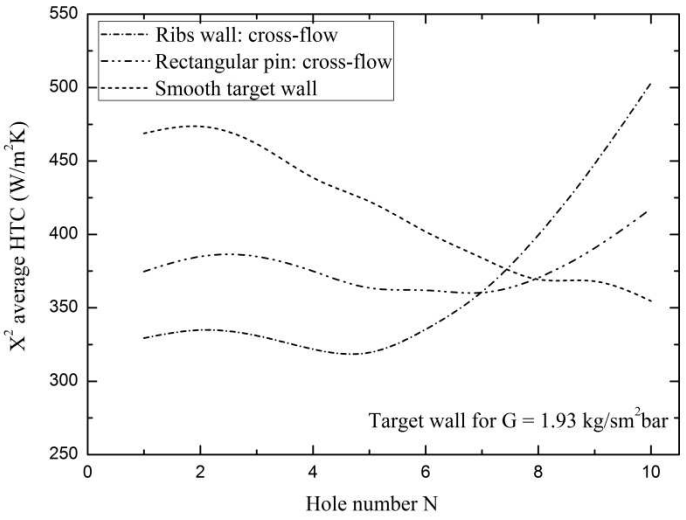

Figure 14: Comparison of predicted locally surface average HTC on the target wall for all G of the obstacle geometries

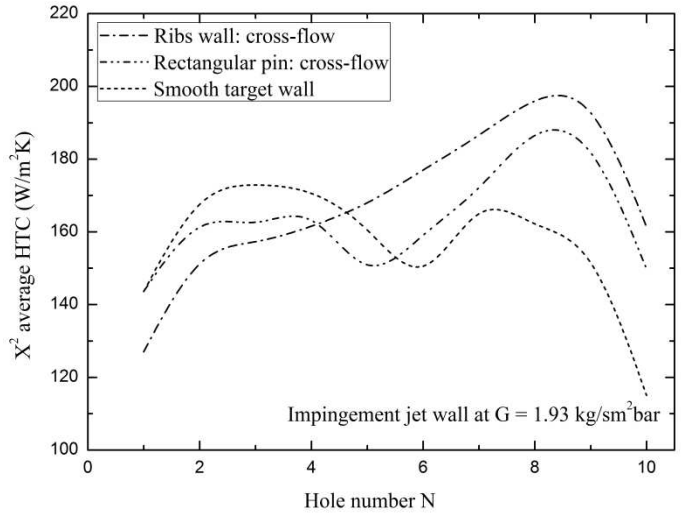

Figure 15: Comparison of predicted locally surface average HTC on the impingement jet wall for obstacle and smooth wall.

Predictions of the Heat Transfer Coefficient (HTC)

The predicted and measured total surface area mean HTC, which is the average of all 10 rows of holes, are shown in Figure 13 as a function of the coolant mass flux, G. The predictions and experiments both show that the continuous rib was superior to the rectangular pins. For the predictions the difference was 12% at low G and 5% at high G, compared with the experimental difference of 10% at low G and no difference at high G. However, the absolute values of the predicted HTCs were below those of the measurements by 12% for the rectangular pins at low G and 8% at high G and for the ribs 6% at low G and 4% at high G. This is quite good agreement for the conjugate heat

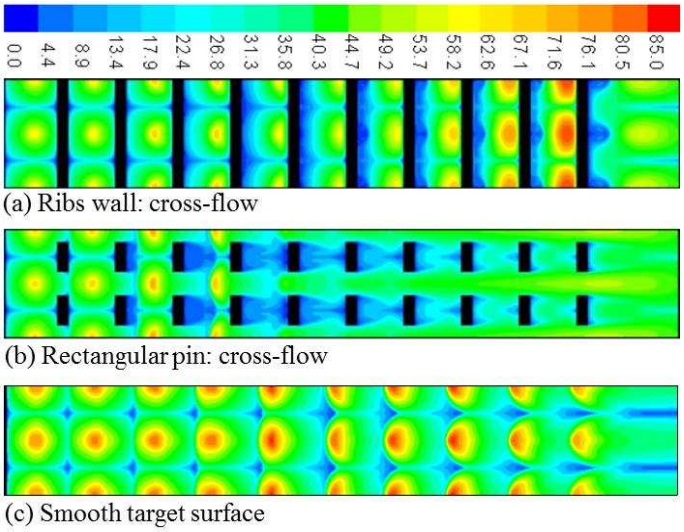

Figure 16: Comparison of Nusselt number contours for enhanced target and smooth surfaces for G of 1.93 kg/sm^{2}bar

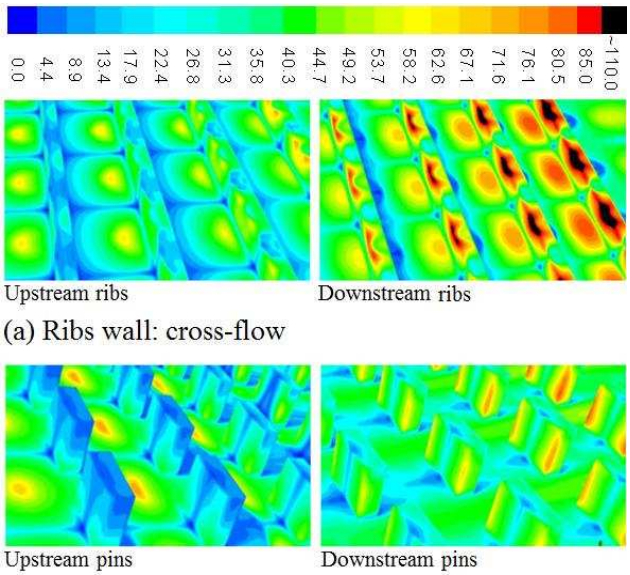

Figure 17: Nusselt number contours on the target surface and the obstacle walls for G 1.93 kg/sm^{2}bar

transfer CFD and for the continuous fins was within the experimental error bands.

Figure 14 shows the axial variation of the individual impingement jet locally surface averaged HTC over the X^2 surface area cooled by each jet for holes 1-10 in the crossflow direction. Figure 14 shows that this is a massive effect and is strongly different for the smooth wall from the obstacle walls. The reason is due to the flow maldistribution differences discussed above in relation to Figure 7. This shows that for a smooth wall the flow maldistribution between the first and last holes was 20% but was much higher for both the obstacle walls,

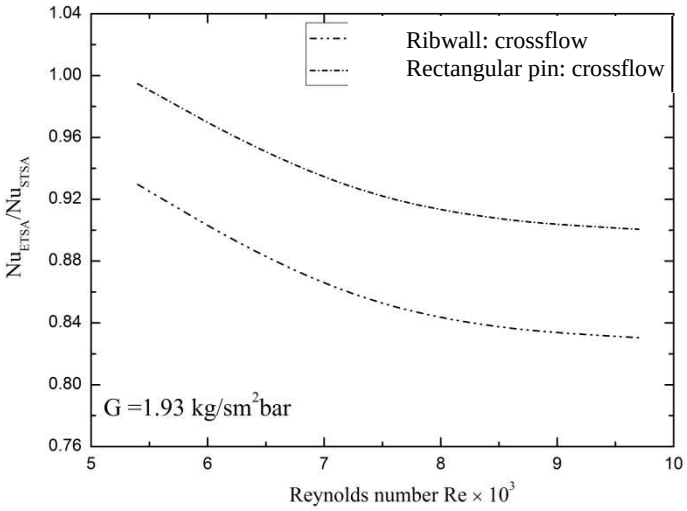

Figure 18: Comparison of enhanced target surface predicted surface average Nu over smooth average Nu versus Re

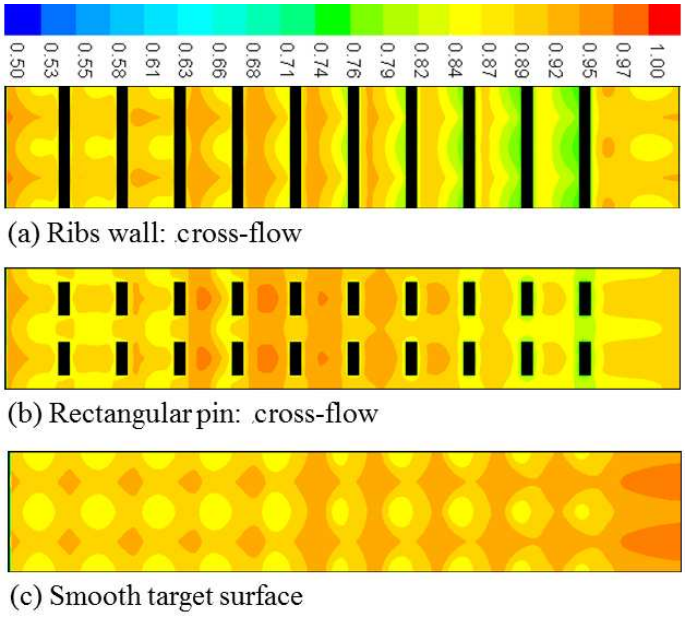

Figure 19: Comparison of normalized temperature contours for enhanced and smooth surfaces for G of 1.93 kg/sm^{2}bar.

but was greatest for the ribbed wall. The consequences, of a low impingement coolant mass flow in the first rows of holes and high in the last, is that this is also the axial trend for the HTC. This effect is significantly worse for the continuous ribbed obstacle than the rectangular pins obstacle and both were much worse than for the smooth wall. These strong gradients in the local X^2 average HTC are undesirable as they will lead to strong wall temperature gradients. They were also much worse than for the same obstacles in the co-flow orientation [7]. The agreement of CFD and experiments was also much better, with no significant differences of HTC for the co-flow [8]. As there is no advantage of the more complex aerodynamics of the crossflow

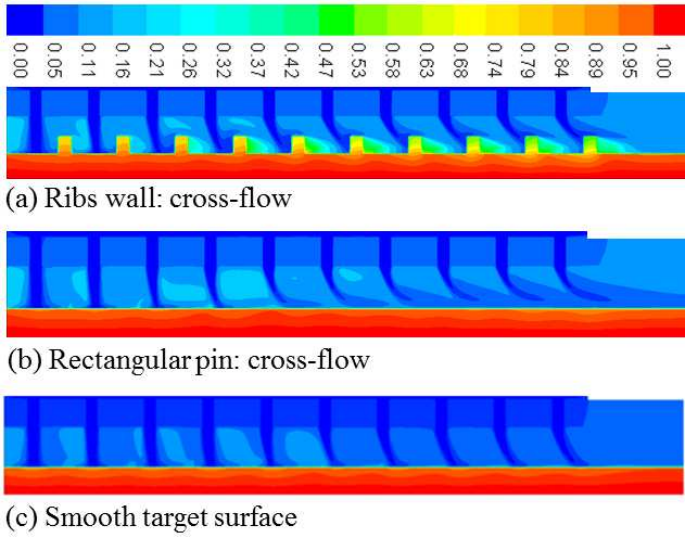

(i) Rows of half holes plane for G of 1.93 kg/sm^{2}bar

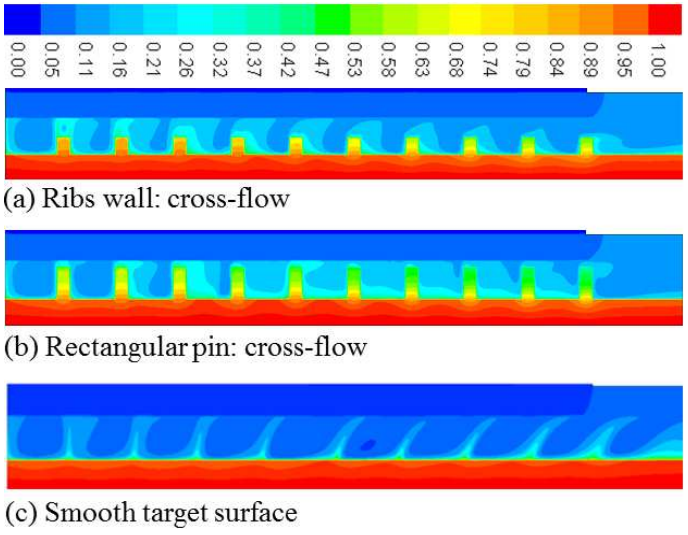

(ii) Plane between rows of holes for G of 1.93 kg/sm^{2}bar

Figure 20: Comparison of normalized temperature contours in the impingement gap for cross-flow obstacles with smooth wall

configuration in terms of higher overall coolant heat transfer then this configuration cannot be recommended for the current application of regenerative combustor cooling.

The impingement gap has two surfaces and the heat transfer to the impingement jet wall is part of the overall heat transfer, as the heat removed from the target wall is transferred to the impingement jet wall and then by heat transfer to the coolant air passing through this wall. The CHT CFD model enables the HTC for the impingement jet wall to be predicted and the results are shown in Figure 15. The predictions show a similar magnitude for the HTC for all 3 designs but with the smooth wall having the highest value for the first few impingement jets and the continuous ribbed wall the highest for the downstream

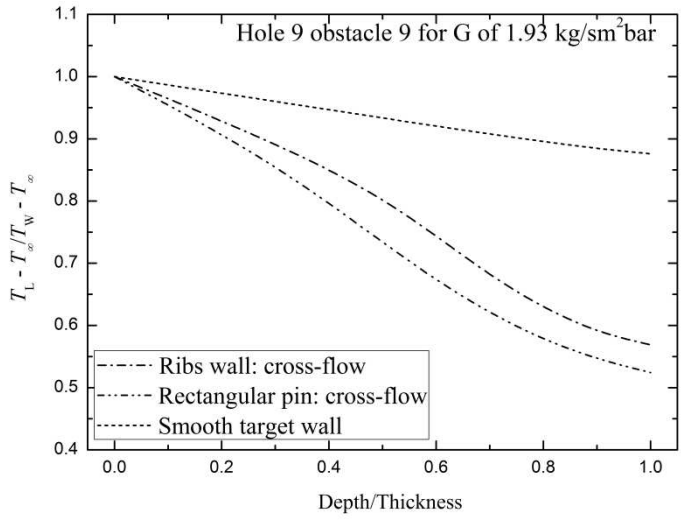

Figure 21: Predicted normalized thermal gradient from target wall hot side through the obstacle walls compared with smooth wall for G of 1.93 kg/sm^{2}bar

holes. The impingement jet heat transfer is predicted to be about one third of the target wall for smooth walls and 50% for the fin and pin obstacle walls for the first few holes and then a higher proportion for the last few holes. Part of the action of the rib and the pin obstacle is to deflect the cross flow onto the impingement jet surface instead of the target surface, with a reduced target surface cooling as a consequence.

Predictions of the Surface Distribution of Nu

Figure 16 shows the predicted target surface distribution of the Nu. The smooth wall had an area of high Nu in line with the impingement jets. The area of high Nu reduced for the downstream impingement holes and this was reflected in the reduced overall locally surface average HTC in Fig. 14. The continuous rib obstacles had reduced Nu in line with the jets in the upstream part of the surface due to the higher flow maldistribution. However, as the crossflow built up the higher impingement jet target Nu was offset by the crossflow wake region behind the rib having near zero Nu. This negative impact of the obstacles on the target surface heat transfer was even worse for the rectangular ribs in crossflow as there was no target surface jet impingement after row 4 and wake region downstream of each pin after row 4 was near zero Nu. This illustrates the reason for the poor performance on this cross flow arrangement of the fin and pin obstacles. In contrast the co-flow arrangement of obstacles [7] did not stop the normal impingement jet cooling of the target surface, nor were any wake regions of low Nu created by the crossflow.

The Nu contours on the rib and pin surfaces are shown in Figure 17 and this further emphasises the poor performance of the pins. For the continuous ribs the impingement jets do interact with the rib and give regions of high Nu on the upstream surface, but in the upstream impingement holes the reduced area of high Nu compared with the smooth wall gives the lower overall heat transfer discussed above. In the downstream jets the crossflow effects are very strong, which combined with the high flow maldistribution results in extremely high Nu locally on the fin. This is the cause of the very high overall HTC shown in Figure 14. The pin obstacles in Figure 18 show the disastrous influence of the pins as there are few regions of high Nu for upstream or downstream jets and the good heat transfer advantages of the smooth wall impingement cooling have been destroyed by the location of the pins. The increased crossflow velocity in the gap between the pins proved not to be an enhancing feature in the heat transfer, but was a destroyer of the impingement jets and prevented them from reaching the target surface in the downstream region of the wall.

The surface averaged Nu, including the surface of the ribs and pins, as a ratio of the smooth wall impingement surface averaged Nu is shown in Figure 18 as a function of the impingement jet Re. This shows that for both the ribs and pins overall the action of the obstacles in crossflow was to reduce the average surface Nu for all jet Re or G. This shows that there was no benefit of either of the ribs in crossflow. There were only problems, such as higher pressure loss and increased flow maldistribution created by the obstacles. Overall the rectangular pins had lower surface averaged heat transfer than the continuous ribs in crossflow, but both configurations were worse than for a smooth wall. In contrast, the previous CHT CFD predictions [7] for the same obstacles with co-flow alignment of the ribs and pins showed an improved surface average Nu of 7% at low G and the continuous ribs were more effective than the row of rectangular pins.

Dimensionless Wall Temperature Profiles

The dimensionless wall temperature T^* in Eq.2 enables the thermal gradients on the surface of the metal wall to be predicted. These are controlled by the internal metal wall heat conduction as well as the surface distribution of the Nu. The predicted surface distribution of T^* is shown in Fig. 20 which

$$T^* = \frac{(T - T_\infty)}{(T_w - T_\infty)} \qquad (2)$$

shows a similar picture to the Nu distribution in Figure 16, with the coolest wall beneath the highest Nu location and this is also the location of peak TKE in Figure 12. However, due to internal wall conduction, the surface gradients in T^* are much lower than the surface gradients in Nu or TKE. For the smooth wall and the pin fin wall the thermal gradients were 5% of the difference in hot side wall temperature and the coolant. For the continuous ribs the gradient was 8% in the downstream region, where the crossflow was most important. This was the original assumption in the experimental work, that the wall temperature measured at the furthest distance from the impingement point would be a conservative measure of the mean surface temperature and could be used in a transient cooling test to determine the surface averaged heat transfer coefficient. These predictions justify the assumptions in this use of the lumped capacitance method for determining the surface averaged HTC.

Eq. 2 gives the thermal gradient for the metal profiles, but if used for the coolant gas as the local temperature T, then T^* for the coolant gives a prediction of the heating of the cold impingement jets and can also visualise the hot reverse flow jet. This is shown in Figure 20i for the vertical plane through the centreline of the impingement jet holes and in Figure 20ii on the plane midway between the impingement holes. In the metal wall the thermal gradients through the thickness of the wall are shown as well as the thermal gradients in the ribs and pins. For the smooth wall these are 11% between the cooled top surface and the heated bottom surface. However, when the ribs and pins are added the thermal gradients in the ribs and pins are very large and are 50% from the top of the pin to the hot metal surface, as shown in Figure 20ii. This further emphasises how unsuitable is this design for practical use. These thermal gradients in the metal are shown in Figure 21 for the dimensional metal distance, where the distance for the pins is the greatest. This summarises how strong the thermal gradients are when ribs and pins are used in crossflow compared with the smooth impingement target wall.

The T^* profiles for the coolant in Figure 20i clearly show the flow direction of the cold impingement jet and its deflection as the crossflow increases. It also shows the heated flow on the hot metal surface due to the heat transfer. This then results in the hot reverse flowing jets in Figure 20ii for the flow between the impingement jets. With the ribs and pins the crossflow is higher and the impingement jets are deflected to hit the ribs for the downstream impingement jets. This also gives the very high Nu on the ribs shown in Figure 17a.

Figure 20 shows that for the ribs the impingement jet does not reach the target surface after the fourth impingement jet. For the last 6 jets the impingement flow hits the ribs and these then conduct heat from the target surface. For the pins the higher crossflow between the pins deflects the impingement jet significantly and there is no direct impingement of the jets on the target surface after the fourth row of jets. For the ribs Figure 20i shows that hot gases are entrained in the recirculation zone downstream of the ribs and this deteriorates the target surface cooling. Figure 20 shows much simpler and effective cooling of the target surface for the smooth wall. There are still problems with the interaction with the crossflow, but these are much less than for the rib and pin crossflow geometries.

CONCLUSIONS

CHT CFD predictions for obstacle enhanced impingement heat transfer were carried out for G of 1.08, 1.48 and 1.93 kg/sm^{2}bar at a fixed X/D of 4.66 and Z/D of 3.06. The predictions showed good agreement with the experimental surface and locally X^2 averaged HTC. Also, the predictions of the pressure loss were in good agreement with the measurements, indicating that the aerodynamics were adequately predicted.

The predictions showed that it was difficult to enhance the smooth wall impingement heat transfer and that obstacles could deteriorate the heat transfer. The main effect of the obstacles was to enhance the heat transfer to the impingement jet wall and decrease it to the target wall, relative to a smooth wall. Small increases in the overall surface averaged heat transfer were predicted for the upstream jets for the cross-flow configuration with ribs, but were not significant.

For the ribs the impingement jet was predicted not reach the target surface after the fourth impingement jet. For the last 6 jets the impingement flow hits the ribs and these then conduct heat from the target surface. For the pins the higher crossflow between the pins deflects the impingement jet significantly and there was no direct impingement of the jets on the target surface after the fourth row of jets.

For both the ribs and pins overall the action of the obstacles in crossflow was to reduce the average surface Nu for all jet Re or G. This shows that there was no benefit and only problems, such as higher pressure loss and increased flow maldistribution created by the obstacles. Overall, the ribs were worse than the pins but neither were an improvement on the smooth wall surface averaged heat transfer. In contrast the previous CHT CFD predictions [7] for the same obstacles with co-flow alignment of the ribs and pins with the crossflow showed a small improvement in the surface average heat transfer. The improved surface average Nu was predicted to be 7% at low G and the continuous ribs were more effective than the row of rectangular pins. This better performance of the co-flow configuration was also in agreement with the experimental measurements [7]. The co-flow configuration also had a lower increase of the smooth wall pressure loss and lower flow maldistribution than for the present crossflow configuration [7].

ACKNOWLEDGEMENTS

Abubakar M. El-jummah wishes to acknowledge the financial support from University of Maiduguri and the Government of Nigeria. We would like to thank the University of Leeds for the provision of computing facilities.

REFERENCES

[1] Abubakar M. El-Jummah, Ahmad Nazari, Gordon E. Andrews, John E. J. Staggs, 2017. Impingement/Effusion Cooling Wall Heat Transfer: Reduced Number of Impingement Jet Holes Relative to the Effusion Holes. Proceedings of the ASME Turbo Expo:Turbomachinery Technical Conference & Exposition GT2017 June 26 - 30, 2017, Charlotte, North Carolina, USA. ASME GT2017-63494

[2] Reiss F., Wiers S-H., Orth U., Aschenbruck E., Lauer M. & El Masalme J. 2014. Combustion System Development and Testing for MAN's New Industrial Gas Turbines MGT 6100 and MGT 6200. Proc. ASME Turbo Expo, GT2014-25907.

[3] Kercher D. M. and Tabakoff W. 1970. Heat Transfer by a Square Array of Round Air Jets Impinging Perpendicular to a Flat Surface Including Effect of Spent Air. Trans. ASME J.

Eng. Power, 73 - 82.
[4] El-jummah A. M., Abdul Hussain R. A. A., Andrews G. E. and Staggs J. E. J. 2014. Conjugate Heat Transfer Computational Fluid Dynamic Predictions of Impingement Heat Transfer: The Influence of Hole Pitch to Diameter Ratio X/D at Constant Impingement Gap Z. Trans. ASME J. Turbomachinery, 136 (12), 1 - 16.
[5] Bunker R. S. 2008. The Effects of Manufacturing Tolerances on Gas Turbine Cooling. Proc ASME Turbo Expo, 2008-GT-50124, 1 - 16.
[6] Tapinlis O., Choi M., Gillespie D. R. H., Lewis L. V. and Ciccomascolo C. 2014. The Effect of Impingement Jet Heat Transfer on Casing Contraction in a Turbine Case Cooling System. Proc. ASME Turbo Expo, 2014-GT-26749, 1 - 11.
[7] El-jummah A. M., Andrews G. E. and Staggs J. E. J. 2016. Impingement Jet Cooling with Ribs and Pin Fin Obstacles in Co-flow Configurations: Conjugate Heat Transfer Computational Fluid Dynamic Predictions. Proc. ASME Turbo Expo: Turbomachinery Technical Conference & Exposition, 2016-GT- 57021, 1 - 15.
[8] El-Jummah, A.M., Oluwole, F.A., Andrews, G.E and Staggs, J.E.J.m 2017. "Numerical Predictions of Enhanced Impingement Jet Cooling with Ribs and Pins in Co-Flow an Cross-Flow Configurations" Arid Zone Journal of Engineering, Technology and Environment, February, 2017, Vol(13) : 149-162
[9] Andrews G. E. and Hussain C. I. 1987. Full Coverage Impingement Heat Transfer: The Influence of Cross-Flow. AIAA/SAE/ASME/ASEE 23rd Joint Propulsion Conference, AIAA-87-2010, 1 - 9.
[10] El-jummah, A. M., Abdul Hussain R. A. A., Andrews G. E. and Staggs J. E. J. 2013. Conjugate Heat Transfer CFD Predictions of the Surface Averaged Impingement Heat Transfer Coefficients for Impingement Cooling with Backside Cross-flow. Proc. ASME IMECE Conference, 2013-IMECE-63580, 1 - 14.
[11] El-jummah, A. M., Andrews, G. E. and Staggs, J. E. J. 2013. Conjugate Heat Transfer CFD Predictions of Impingement Jet Array Flat Wall Cooling Aerodynamics with Single Sided Flow Exit. Proc. ASME Turbo Expo Conference,2013- GT-95343, 1 - 12.
[12] El-jummah, A. M., Andrews, G. E. and Staggs, J. E. J. 2013. Conjugate Heat Transfer CFD Predictions of the Influence of the Impingement Gap on the Effect of Cross-Flow. Proc. ASME Heat Transfer Conference, 2013-HT-17180, 1 - 12.
[13] Andrews G. E., Abdul Husain R. A. A. and Mkpadi M. C. 2003. Enhanced Impingement Heat Transfer: Comparison of Co-Flow and Cross-flow with Rib Turbulators. Proc. GTSJ Int. Gas Turbine Congress, IGTC TS-075 1 - 8.
[14] Andrews G. E., Abdul Husain R. A. A. and Mkpadi M. C. 2006. Enhanced Impingement Heat Transfer: The Influence of Impingement X/D for Interrupted Rib Obstacles (Rectangular Pin Fins). Trans. ASME J. Turbomachinery, 128, 321 - 331.
[15] Abdul Husain R. A. A. and Andrews G. E. 1991. Enhanced Full Coverage Impingement Heat Transfer With Obstacle in the Gap. Proc. ASME Int. Gas Turbine & Aeroengine Congress & Eposition, 91-GT-346, 1 - 12
[16] Shizuya M. & Kawaike K. 1987. Experimental Investigation of Blade Internal Cooling Methods Using Ribs and Fins. Proc. GTSJ Int. Gas Turbine Congress, IGTC1987-65, 159 - 166.
[17] Azad G. M. S., Huang Y. & Han J. 2002. Jet Impingement Heat Transfer on Pinned Surfaces Using a Transient Liquid Crystal Technique. Int. J. Rotating Machinery, 8 (3), 161 - 173.
[18] Ligrani P. M., Oliveira M. M. & Blaskovich T. 2003. Comparison of Heat Transfer Augmentation Techniques. AIAA Journal, 41 (3), 337 - 362.
[19] Ligrani P. M. 2013. Review Article: Heat Transfer Augmentation Technologies for Internal Cooling of Turbine Components of Gas Turbine Engines. Hindawi Int. J. Rotating Machinery, 2013, ID. 275653, 1 - 32.
[20] El-jummah A. M., Andrews G. E. and Staggs J. E. J. 2015. Conjugate Heat Transfer CFD Predictions of Metal Walls with Arrays of Short Holes as used in Impingement and Effusion Cooling. Proc. GTSJ Int. Gas Turbine Congress, IGTC TS - 266, 1 - 9.
[21] Andrews, G.E. and Mkpadi, M.C. Full coverage discrete hole wall cooling - discharge coefficients. ASME 83-GT-192, Transactions of the ASME, Journal of Engineering for Power, Vol.106, pp.183-192 (1984).

Correpondence:

G.E.Andrews@leeds.ac.uk
Dr. Abubakar El-Jummah <AMEljummah@hotmail.com>